Strength and Viscosity Effects on Perturbed Shock Front Stability in Metals

S. Opie,[1] E. Loomis,[2] P. Peralta,[1] T. Shimada,[2] and R. P. Johnson[2]
[1]School for Engineering of Matter, Transport and Energy, Arizona State University, Tempe, Arizona 85287, USA
[2]Los Alamos National Laboratory, Los Alamos, New Mexico 87545, USA
(Received 13 October 2016; revised manuscript received 26 February 2017; published 9 May 2017)

Computational modeling and experimental measurements on metal samples subject to a laser-driven, ablative Richtmyer-Meshkov instability showed differences between viscosity and strength effects. In particular, numerical and analytical solutions, coupled with measurements of fed-through perturbations, generated by perturbed shock fronts onto initially flat surfaces, show promise as a validation method for models of deviatoric response in the postshocked material. Analysis shows that measurements of shock perturbation amplitudes at low sample thickness-to-wavelength ratios are not enough to differentiate between strength and viscosity effects, but that surface displacement data of the fed-through perturbations appears to resolve the ambiguity. Additionally, analytical and numerical results show shock front perturbation evolution dependence on initial perturbation amplitude and wavelength is significantly different in viscous and materials with strength, suggesting simple experimental geometry changes should provide data supporting one model or the other.

DOI: 10.1103/PhysRevLett.118.195501

Under nonequilibrium conditions, irreversible thermodynamic processes, such as viscous flow, plastic deformation, and thermal conduction are known to alter the stability of shock waves propagating through an arbitrary fluid or solid. Miller [1] was among the first to investigate these effects using numerical solutions of the conservation equations for a Newtonian fluid. In the inviscid limit, perturbations on the shock front exhibit decaying oscillations with frequency depending on kv where $k = 2\pi/\lambda$, $v = U_s - U_p$ is the shock velocity in a comoving frame and U_s and U_p are the shock and fluid velocities with respect to the material ahead of the shock, respectively. Bates [2] gives the oscillation period as $T \sim \lambda/U_s$, which agrees with [1] in the weak shock limit. With increasing viscosity, deviatoric components of the stress tensor become more important, eventually preventing the modulation in fluid pressure from causing the phase reversal in perturbation amplitude and increasing the delay at which the amplitude reaches zero. While our current understanding of how shock stability is affected by viscosity at high pressures is fairly advanced, to the point that it can be used to measure viscosity of shocked fluids [1,3], our understanding of the role of strength (shear response) on shock stability in solids is still lacking.

Research on inertial confinement fusion (ICF) has shown that shock waves carry nonuniformities from the outer ablation surface during the x-ray radiation drive to inner layers of the capsule creating density modulations in the capsule itself or feeding directly to the inner surface where Rayleigh-Taylor (RT) growth will occur during hot spot formation of the thermonuclear deuterium-tritium fuel [4]. The final depth that the RT fingers reach into the hot spot can closely depend on the amplitude imprinted by the shock front. It is therefore important to understand the role of viscosity on the evolution of shock front nonuniformities since long wavelength modulations can persist deep into the capsule seeding unstable perturbation growth [5]. Highly sensitive measurements of velocity perturbations have revealed ablator non-uniformities and their evolution during shock transit in dense liquid (or plasma) [4]; however, new experimental methods are needed to determine how these velocity perturbations accumulate over time leading to displacement modulations at the ablator inner surface.

Additionally, efficient ablators such as high-density carbon (HDC) and beryllium are looking to advance ICF designs through greater hydrodynamic stability. These ablators possess crystal structures that are currently melted with the first shock, which would otherwise create the potential for instability seeding [6]. In the case of beryllium this first shock pressure is 3 Mbar, which sets the capsule on a moderately high adiabat that reduces its attainable compression. Exploring lower adiabats below the 1st shock melt pressure with beryllium and HDC may prove necessary to approach ignition, which will require the use of material strength models in ICF design simulations to predict the evolution of shock front modulations in finite strength heterogeneous solids. In addition to lower adiabats, 1st shock solid ablators may create conditions leading to favorable modifications to ablative Richtmyer-Meshkov (RM) oscillation periods and decreasing ablation front amplitudes prior to the onset of RT [5].

In this Letter we present experimental results that demonstrate how ablation front modulations are carried through metals possessing finite strength under shear deformation (modulated shock front) and evolve as post-shock displacement modulations on the opposite surface, while accompanying simulations evaluate modern strength model behavior under these conditions, providing insight

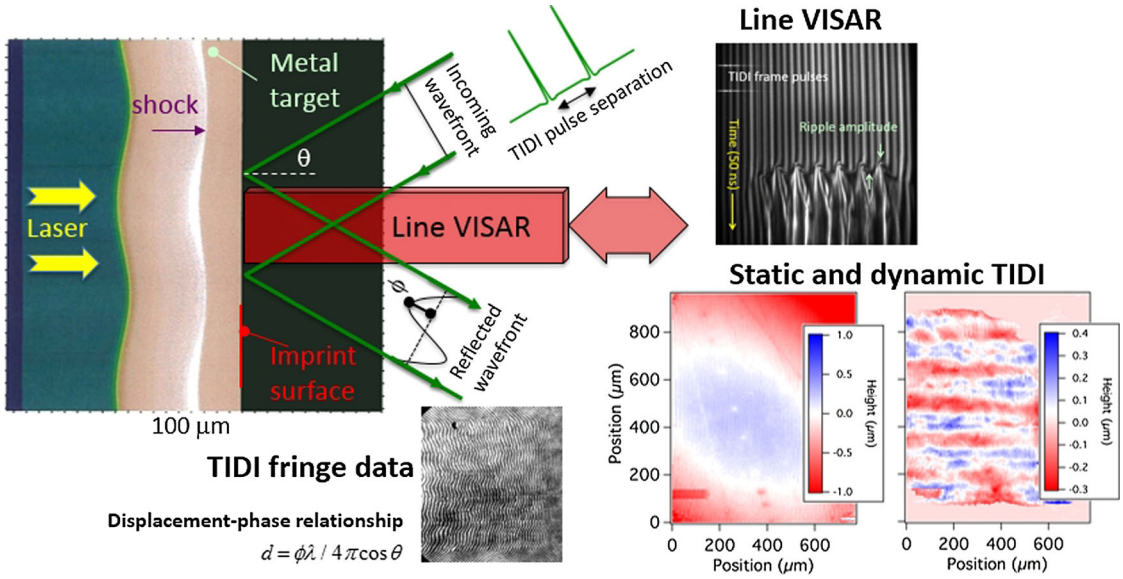

FIG. 1. Illustration of a rippled shock target with example VISAR and TIDI data used to measure shock feedthrough and imprint. The shock ripple oscillation frequency and growth of the imprint at the breakout surface are used to validate strength models that may soon be used in ICF designs to predict ablation front feedthrough in 1st shock solid ablators.

into the different roles that viscosity and strength play on this phenomenon.

Our experiments were based on measurements of displacement and velocity modulations as a rippled shock (generated by opposite rippled surface irradiation) arrived at the measurement surface. This is illustrated in Fig. 1 using a simulation of a sinusoidal geometry experiment with the multiphysics code HYDRA [7] that captures laser or ablation dynamics and was used for early experimental design, while subsequent simulations were performed using the finite element code ABAQUS/EXPLICIT™ [8] to facilitate incorporation of various strength models and postprocessing results. Half-hard oxygen-free high conductivity (OFHC) Cu targets were fabricated using a photolithography technique, primarily due to process availability, to etch one surface with a square wave modulation followed by polishing the opposite surface to a mirrorlike finish. The square wave surface contains a spectrum of discrete peaks in Fourier space where the fundamental mode has the wavelength of an equivalent period sinusoid and is followed by an infinite series of exponentially decaying harmonics. Since the shock front oscillation frequency is (approximately) linearly proportional to k_0 then all the harmonics decay to zero in half the time (or distance) in which the fundamental mode oscillates to zero. Hence, the shock front perturbation behaves as a single mode over extended distances. This was an important consideration when selecting target thicknesses.

Rippled shocks were generated using 10–30 J square wave pulses of 5 ns duration on the modulated target surface from the TRIDENT laser at Los Alamos National Laboratory (LANL). First harmonic laser light from the Nd: glass front end was converted to 2ω light using monopotassium phosphate (KDP) crystals prior to entering the target chamber. Laser pulses were focused to a 1 mm × 1 mm square spot on the target using a distributed phase plate creating intensities on the target of 4×10^{11} W/cm^2. When the laser first illuminates the modulated surface blow-off plasma creates a separation between the critical surface where the laser is absorbed and the ablation front separating plasma from shocked solid material. With modulations on the ablation front this scenario quickly sets up the conditions for the ablative RM effect first observed by [9] and derived theoretically by [10]. When generated in a metal, however, shear flow induced by pressure modulations behind the shock front is opposed by the resulting shear stresses in contrast to inviscid fluids [11]. Note also that any ablation variation (at our power levels) caused by the surface perturbations will be a higher order effect that should not affect the fundamental mode decay over extended distances [12].

In these experiments we investigated two different initial surface perturbation wavelengths (80 and 150 μm ± 5.0 μm with amplitudes of 5 to 6 μm ± 0.25 μm) to study shock perturbation amplitude (i.e., spatial difference between shock fronts in sample) evolution and to study the ensuing dynamic evolution of the postshock imprint at the initially flat breakout surface. The shock front perturbation, as it broke out at a free surface, was recorded for several sample thicknesses to determine perturbation evolution with distance traveled Δx. Breakout times were measured using a line-imaging velocity interferometry system (VISAR [13]) that spatially resolved across several shock front ripples (approximately 1 mm field of view and 10 μm resolution). An example of typical VISAR rippled shock data is shown in Fig. 1. Most target thicknesses

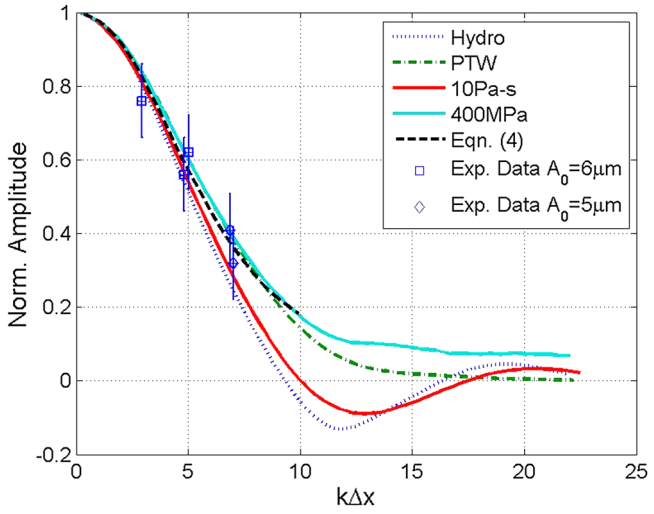

FIG. 2. Shock front perturbation amplitude experimental data and their comparison to inviscid (Hydro), viscous (10 Pa s), elastic-plastic (400 MPa), and PTW material models. Simulations are for a 150 μm wavelength and a $A_0 = 6$ μm initial amplitude.

(Δx, ~50 to ~200 μm) were chosen such that a clear single mode shock front perturbation would be measured by the VISAR streak camera. The temporal modulation was converted to a spatial amplitude by multiplication with the shock velocity determined from free surface velocity measurements, and a linear U_s-U_p EOS, of separate targets possessing no surface modulation and shot under the same laser conditions (e.g., energy, pulse length). The flat sample VISAR data were also used to convert the laser 5 ns pulse to an equivalent (nonsquare) pressure boundary condition.

The results of five experiments at similar shock conditions (~12 GPa and 150 μm wavelength), where target thickness Δx was varied, are shown in Fig. 2. The error bars are determined by the temporal resolution and noise in the VISAR data. Results at larger $k\Delta x$ values are not included due to perturbation decay being dominated by the shock release wave [14]. In future work, longer laser pulses and thicker samples would be used.

We also show the results of ABAQUS™ simulations, with a 0.5 micron element size mesh (about 1/10 of initial perturbation amplitude to avoid phase shifts in Fig. 2 plots), where a constant 0.3 μm/ns (equivalent to ~12 GPa) velocity was applied to a surface with a perfect sinusoidal modulation (square vs sine perturbation simulations show only minor differences after an initial settling time of approximately half the fundamental mode, and analytically a single sinusoidal geometry is more clearly analyzed). A constant velocity condition was applied to show the decay behavior qualitatively; simulations with release waves did not have an effect on results until the release wave reached the shock front [14]. All simulations used a Mie-Grüneisen equation of state with parameters from [15], but we compare inviscid and viscous fluid solutions to elastic perfectly-plastic and Preston-Tonks-Wallace (PTW) [16] materials possessing strength. PTW model parameters $y_0 = 1 \times 10^{-3}$ and $y_\infty = 1 \times 10^{-5}$ (compare to Ref. [16]) were adjusted to increase flow stress at low strain hardening values to match our free surface VISAR velocity data on flat samples. For the viscous model a shear viscosity of 10 Pa s was selected to best fit the shock front width (i.e., rise time) produced by the PTW model. The elastic perfectly-plastic model was given a yield stress of 400 MPa, which was the approximate average flow stress found in the shocked region of the PTW model simulations. These material model parameters were derived from flat sample data; all perturbed sample simulations are predicted using the above material parameters.

Figure 2 shows that all the models qualitatively match the perturbed shock front data well, although they differ as the shock perturbation nears inversion, with the strength models predicting no inversion at all. It should be noted that the shock perturbation amplitudes in Fig. 2 were generated by finding the spatial position difference between two particles on the shock fronts that had a particle velocity twice that of the elastic precursor (~0.05 μm/ns). The viscous results in Fig. 2 were sensitive to this definition, but consistently showed inversion in all cases. Despite the fact that the experimental VISAR data do not have $k\Delta x$ values large enough to show the predicted difference after inversion, we will show later that highly sensitive displacement measurements of ripple imprint on the back surface can be used to provide additional material validation information.

To provide additional insight on the role of strength as it pertains to shock front stability up to and near shock front inversion, we present the following semi-analytical model. Zaidel [17], and later Miller [1], used an approximate solution for the shock perturbation amplitude $A(t)$ of a viscous fluid $A(t) = A_{\text{hydro}}(t) + A_{\text{pert}}(t)$, where A_{hydro} is the inviscid fluid solution and A_{pert} is a perturbation caused by the viscosity. We propose a similar form. Consider that the intensive properties just behind the shock front are comprised of a zeroth order term, which would be the result of a steady shock wave, and a perturbed term, e.g., for the longitudinal velocity we have $v_x = v_{x0} + v_x'$ [1]. Then the equations of motion just behind the shock front, after eliminating second order perturbed terms and noting that deviatoric terms are saturated in the shock direction x, are

$$\frac{\partial v_x'}{\partial t} + v_{x0}\frac{\partial v_x'}{\partial x} + \frac{1}{\rho}\frac{\partial P'}{\partial x} = \frac{1}{\rho}\frac{\partial S_{xy}}{\partial y} + \frac{1}{\rho}\frac{\partial S_{xx}}{\partial x} \approx \frac{1}{\rho}\frac{kY}{\sqrt{3}} + 0, \tag{1}$$

$$\frac{\partial v_y'}{\partial t} + v_{x0}\frac{\partial v_y'}{\partial x} + \frac{1}{\rho}\frac{\partial P'}{\partial y} = \frac{1}{\rho}\frac{\partial S_{yy}}{\partial y} + \frac{1}{\rho}\frac{\partial S_{yx}}{\partial x} \approx \frac{-i}{\rho}\frac{kY}{\sqrt{3}} + 0, \tag{2}$$

where S_{ij} is the deviatoric stress, Y is the material yield stress, and we assume perturbed terms vary in the y direction with $\exp(iky)$, to account for their periodicity.

TABLE I. Experimental peak-to-valley TIDI surface data for shots 25 288 and 25 289 and simulation predictions. Amplitudes are taken 6.2 and 7.0 ns after leading shock breakout, respectively.

Time (ns)	Experimental (μm)	Hydrodynamic (μm)	Viscous (μm)	Elastic-Plastic (μm)	PTW (μm)
6.2 ± 0.5	0.20 ± 0.05	0.37	0.35	0.26	0.22
7.0 ± 0.5	0.33 ± 0.05	0.53	0.50	0.39	0.32

The terms on the right-hand side in Eqs. (1) and (2) represent the difference between an inviscid material and materials with strength. Along a peak or valley the perturbation amplitude is

$$A(t) = -\int_0^t U_s'(t)dt = -s\int_0^t v_x'(t)dt, A(0) = A_0,$$
$$dA/dt|_{t=0} = 0, \tag{3}$$

where we have used a linear relationship for the shock velocity perturbation $U_s' = sv_2'$. The right-hand side of Eq. (1) is of opposite sign to the instantaneous value of v_x', then the strength delays the perturbation decay and an estimate for $A(t)$ before inversion is

$$A(t) = -s\int_0^t v_x'(t)dt \approx A_{\text{hydro}}(t) + \frac{1}{2}\frac{U_{s0} - v_{20}}{U_{s0}}\frac{1}{\rho_0}s\beta k\frac{Y}{\sqrt{3}}t^2, \tag{4}$$

where the second term on the right-hand side is an estimate for A_{pert} before shock inversion, and we have assumed small density perturbations, i.e., $v_{20}/U_{s0} \approx 1 - \rho_0/\rho$. We find that the fitting factor $\beta \approx 0.7$ produces good results across a wide range of pressures, geometries, and strengths if the approximate limits $A_0/\lambda < 0.05$ and $PA_0/\lambda > Y$ (P is mean shock pressure) are met and qualitatively beyond these limits [17]. Predictions of Eq. (4), with $A_{\text{hydro}}(t)$ obtained from numerical simulations without strength and with $Y = 400$ MPa, are included in Fig. 2 until the simulations no longer showed yielding at the shock front inflection points, at which point Eq. (4) is invalid.

A result of Eq. (4) is that care needs to be taken when normalizing experimental perturbation results. In inviscid fluids various geometries will fall on a single perturbation curve for a given shock intensity. For viscous materials the normalization in Fig. 2 leaves a factor of η/λ (where η is viscosity) in the analytical solution of Refs. [1,17]. Hence, an increase in wavelength will push a point down in Fig. 2. For materials with strength a factor of $Y\lambda/A_0$ is left so that an increase in wavelength or initial perturbation amplitude pushes a point up or down, respectively [18]. This suggests sources of deviatoric stress could be validated through initial perturbation amplitude or wavelength changes (we were unable to show this due to a lack of larger $k\Delta x$ values). PTW simulations showed the same approximate dependence on λ/A_0 within the limits mentioned and qualitatively beyond those limits. As a final note, if Miller's [1] Eq. (49) is replaced with our Eqs. (1) and (2) then the $Y\lambda/A_0$ factor can be verified with his analytical procedure as well with excellent agreement to ABAQUS™ simulations.

We next look at displacement data obtained from transient imaging displacement interferometry (TIDI) [19,20] that measured the evolution of the free surface with shock breakout. In these experiments a series of 80 ps probe pulses from the TRIDENT front end were relayed to the shock breakout surface with a pulse separation of 6.5 ns. Changes in surface height topology led to local phase shifts (via optical path length changes) in the target arm of the TIDI Mach-Zehnder interferometer, which produced fringe shifts at the image plane. Two gated, intensified single frame Princeton Instruments (PI-Max 2) cameras were placed at equivalent, but separated image planes created by a 50/50 beam splitter where each camera was timed to capture a separate TIDI probe pulse. An example of raw TIDI data showing the periodic phase shift pattern from the breakout of a rippled shock front is shown in Fig. 1. This surface started as mirrorlike, where the fringes were initially straight and vertical. The phase is extracted using the method of Ref. [21] and then the phase displacement relationship shown in Fig. 1 is applied to provide relative surface heights, one static and two dynamic. Surface height maps for a 150 μm wavelength shock ripple given in Fig. 1 show this technique can resolve height features down to ~50 nm, and is preferred over integrating VISAR data that can accumulate appreciable errors [15]. A more thorough description of the instrument and analysis of TIDI fringe patterns can be found in Ref. [15].

Table I lists the peak-to-valley breakout surface displacement data obtained from the first TIDI frame of TRIDENT shot 25 288 and 25 289 ($k\Delta x \sim 5$, $A_0 = 6$ μm, $\Delta x = 120$ μm, 12 GPa) and compares it to the viscous (10 Pa s), elastic-plastic (400 MPa) and PTW model. The only difference between these two shots is the timing of the first TIDI frame capture relative to shock breakout, where the first frame was taken at 6.2 and 7.0 ns for shots 25 288 and 25 289, respectively. As can be seen in Table I, the viscous model is significantly off when compared to the experimental data and strength models. The error in the viscous model stems from weak viscous stress as the shock breaks out at the free surface, as shown in Fig. 3, particularly after arrival (~2.5 ns after leading shock breakout) of the stronger shock front produced at the thicker section of the sample. By comparison, the models with strength produce strong deviatoric gradients

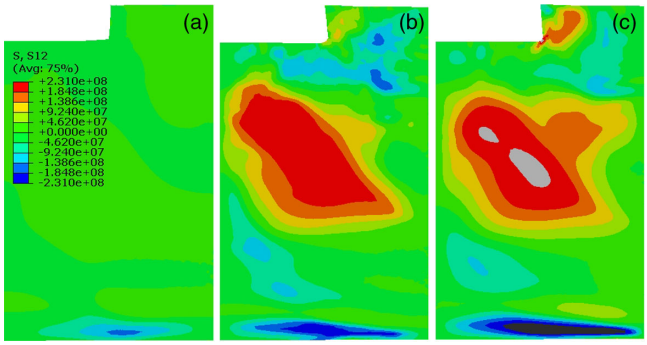

FIG. 3. Comparison of shear stresses after trailing shock front breakout. (a) 10 Pa s, (b) elastic-plastic, and (c) PTW. Stress contour plots (±231 MPa) are linear with units of Pascals.

and in this case the saturated longitudinal deviatoric component is relevant since there is a free surface [22]. Increasing the viscosity improved the viscous results, but increased the shock front rise time beyond what experimental VISAR velocity data from flat samples could support. Rise times in the flat samples were around 1.2, 1.0, and 1.7 ns for the experimental data, PTW model, and 10 Pa s model, respectively, with uncertainties near ±0.2 ns, and doubling the viscosity approximately doubled the rise time. Shock front rise time in the elastic-plastic model (∼0.4 ns) is limited by artificial viscosity, but outside of this brief high strain event the elastic-plastic model matches the deviatoric stress generated in the PTW model better than the viscous model. Similar agreements between elastic-plastic and more complicated material models were observed in other recent instability studies [23].

In summary, we have shown an approach to validate models of deviatoric strength of post-shock material with a simple method that does not need radiographic diagnostics typical of RM type experiments. However, RM, and particularly RT experiments [24] are likely to provide important validation data for material states that are not possible with the experiments detailed in this work (e.g., ramp loading to avoid shocks). Of particular future interest are the shock perturbation front studies, that with optimized [25] diagnostics (in the sense that they should provide better measurements of shock breakout) show promise as a simple method for deviatoric strength validation after the passage of a shock event. Additionally, we have shown with numerical and semi-analytical approaches that shear strength origins, e.g., viscosity or elastic strength, in the postshocked material have the potential to be validated from these shock perturbation measurements by varying simple sample characteristics, such as the initial perturbation amplitude or wavelength.

This work was performed under the auspices of the U.S. Department of Energy's Offices of Fusion Energy Sciences (OFES) under Grant No. DE-SC0008683, National Nuclear Safety Administration under Grant No. DE-NA0002005, and of the Office of Naval Research under Grant No. N00014-16-1-2532 at Arizona State University and an agreement between OFES and LANL. Access to the Trident facility at LANL is gratefully acknowledged.

S. O. and E. L. contributed equally to this work.

[1] G. Miller and T. Ahrens, Rev. Mod. Phys. **63**, 919 (1991).
[2] J. Bates, Phys. Rev. E **69**, 056313 (2004).
[3] X.-J. Ma, B.-B. Hao, H.-X. Ma, and F.-S. Liu, Chin. Phys. B **23**, 096204 (2014).
[4] J. Lindl, Phys. Plasmas **2**, 3933 (1995).
[5] J. L. Peterson, D. S. Clark, L. P. Masse, and L. J. Suter, Phys. Plasmas **21**, 092710 (2014).
[6] A. Mackinnon *et al.*, Phys. Plasmas **21**, 056318 (2014).
[7] M. Marinak, S. Haan, T. Dittrich, R. Tipton, and G. Zimmerman, Phys. Plasmas **5**, 1125 (1998).
[8] ABAQUS, Finite Element Code, Version 6.14 (Dassault Systèmes Simulia Corp., Providence, RI, USA, 2014).
[9] Y. Aglitskiy, A. L. Velikovich, M. Karasik, V. Serlin, C. J. Pawley, A. J. Schmitt, S. P. Obenschain, A. N. Mostovych, J. H. Gardner, and N. Metzler, Phys. Rev. Lett. **87**, 265001 (2001).
[10] V. N. Goncharov, Phys. Rev. Lett. **82**, 2091 (1999).
[11] A. Lopez Ortega, D. J. Hill, D. I. Pullin, and D. I. Meiron, Phys. Rev. E **81**, 066305 (2010).
[12] R. Ishizaki and K. Nishihara, Phys. Rev. E **58**, 3744 (1998).
[13] L. Barker and R. Hollenbach, Rev. Sci. Instrum. **36**, 1617 (1965).
[14] J. G. Wouchuk and J. Lopez Cavada, Phys. Rev. E **70**, 046303 (2004).
[15] E. Loomis, J. Hammerberg, J. C. Cooley, T. Shimada, R. P. Shimada, R. P. Johnson, P. Peralta, R. Olson, and G. T. Gray III, J. Appl. Phys. **117**, 185906 (2015).
[16] D. L. Preston, D. L. Tonks, and D. C. Wallace, J. Appl. Phys. **93**, 211 (2003).
[17] R. M. Zaidel, J. Appl. Mech. Tech. Phys. **8**, 20 (1967).
[18] T. J. Vogler, J. Dyn. Behav. Mater. **1**, 370 (2015).
[19] S. R. Greenfield, D. Swift, and A. Koskelo, in *Shock Compression of Condensed Matter*, edited by M. Furnish, Y. Gupta, and J. Forbes (American Institute of Physics, New York, 2003), p. 1269.
[20] S. R. Greenfield, S. N. Luo, D. Paisley, E. Loomis, D. Swift, and A. Koskelo, in *Shock Compression of Condensed Matter*, edited by M. Elert, M. Furnish, R. Chau, N. Holmes, and J. Nguyen (American Institute of Physics, New York, 2007), p. 1093.
[21] M. Takeda, H. Ina, and S. Kobayashi, J. Opt. Soc. Am. **72**, 156 (1982).
[22] A. R. Piriz, J. J. Lopez Cela, N. A. Tahir, and D. H. H. Hoffmann, Phys. Rev. E **74**, 037301 (2006).
[23] A. Lopez Ortega, M. Lombardini, D. I. Pullin, and D. I. Meiron, Phys. Rev. E **89**, 033018 (2014).
[24] H. S. Park, B. A. Remington, R. C. Becker, J. V. Bernier, R. M. Cavallo, K. T. Lorenz, S. M. Pollaine, S. T. Prisbey, R. E. Rudd, and N. R. Barton, Phys. Plasmas **17**, 056314 (2010).
[25] P. M. Celliers, D. K. Bradley, G. W. Collins, D. G. Hicks, T. R. Boehly, and W. J. Armstrong, Rev. Sci. Instrum. **75**, 4916 (2004).